PAPER

Check for updates

Low bandgap conjugated polymers based on thiadiazoloquinoxaline for high performance shortwave infrared photodetection

Nathan Yee,†[a] Tyler Davidson-Hall,†[a] Neil Graddage,[a] Barbara Martin,[a] Jianying Ouyang, ID [a] Philippe Berrouard[b] and Jianping Lu ID *[a]

The detection of light in the second near-infrared (NIR-II) region of the electromagnetic spectrum is critical for various applications such as bioimaging, environmental sensing and health monitoring. However, the narrow band gaps of organic semiconductors required for NIR-II photodetection increase the probability of charge injection under bias voltages and bulk thermal charge generation in the active layer, leading to a large dark current and low external quantum efficiency which results in poor detectivity. In this study, we introduce a series of low band-gap donor–acceptor type alternating conjugated polymers using thiadiazoloquinoxaline (TQ) as electron-withdrawing units and indacenodithiophene (**P1** and **P2**) or propylenedioxythiophene as electron-donating units (**P3–P5**) for NIR-II photodetection. Polymers **P3–P5** have much lower band gaps than **P1** and **P2** due to the stronger intrachain D–A interaction in the former. **P3** and **P5** have excellent solubility in a variety of organic solvents even at room temperature, which greatly facilitates the device fabrication process. The photodiode device based on **P5** exhibited the highest specific detectivity of 2.0×10^{10} Jones at 1200 nm under -1 V bias owing to the significantly low dark current.

Introduction

Near-infrared (NIR) photodetection is essential for enabling a multitude of technological domains such as bioimaging, environmental sensing, health monitoring, night vision, food quality inspection, and optical communications.[1,2] In particular, light in the second NIR window (NIR-II, 1000–1700 nm) possesses unique attributes such as decreased photobleaching and deeper tissue penetration due to diminished absorption and scattering which result in improved imaging contrast.[3,4] Conventional inorganic Si-based photodetectors have a cutoff wavelength of approximately 1100 nm. To extend detection beyond this, other materials such as InGaAs are typically employed, however their widespread deployment is hampered by their high manufacturing cost, resulting from the need to hybridize with a Si readout circuit (ROIC). Additionally, their lack of flexibility can limit form factor. Colloidal quantum dots (CQDs) such as PbS and HgTe can also achieve photodetection in the NIR-II window, but toxicology concerns hinder their practical application. In this regard, organic photodetectors

(OPDs) have emerged as a promising alternative owing to their compatibility with manufacturing *via* high throughput solution processes, enabling facile integration with ROICs.[5,6] The mechanical flexibility of organic semiconductors will enable new form factors, such as wearable electronics. Of note, OPDs also have high absorption coefficients and offer the potential for narrow absorption windows which can be tuned toward specific applications *via* chemical modifications. Nonetheless, OPDs operating beyond 1000 nm (NIR-OPDs) remain relatively scarce due to the limited material availability and synthetic challenges of organic structures with suitably narrow band gaps (E_g). Furthermore, such narrow band gaps increase the probability of charge injection and bulk thermal generation in the active layer leading to large dark currents and poor detectivities.[5,7]

A common strategy for achieving such low band gaps is *via* the design of push–pull type conjugated polymers featuring alternating strong electron-donating units (D) and strong electron-accepting units (A). When the D and A units are in conjugation, their orbital splitting results in a higher HOMO and lower LUMO and thus a contracted E_g. The HOMO is mainly located on the donor unit and the LUMO on the acceptor which allows for both HOMO and LUMO to be controlled. However, lowering the LUMO is generally seen as a more favorable strategy since air oxidation becomes a concern as the HOMO energy is increased.[8,9] Often, the A unit is pro-quinoidal which promotes quinoidal character along the

[a] *Quantum and Nanotechnologies Research Centre, National Research Council of Canada, 1200 Montreal Road, Ottawa, ON, Canada.*
 E-mail: jianping.lu@nrc-cnrc.gc.ca
[b] *Brilliant Matters, 237 Rue de Liverpool, QC, Canada*
† Nathan Yee and Tyler Davidson-Hall contributed equally to this work.

backbone.[10] With this in mind, [1,2,5]thiadiazolo[3,4-g]quinoxaline (TQ) is one of the strongest pro-quinoidal electron-accepting units that is easily functionalized with solubilizing groups, and is thus an ideal candidate to achieve narrow band gap polymers for infrared photodetection.[11–13]
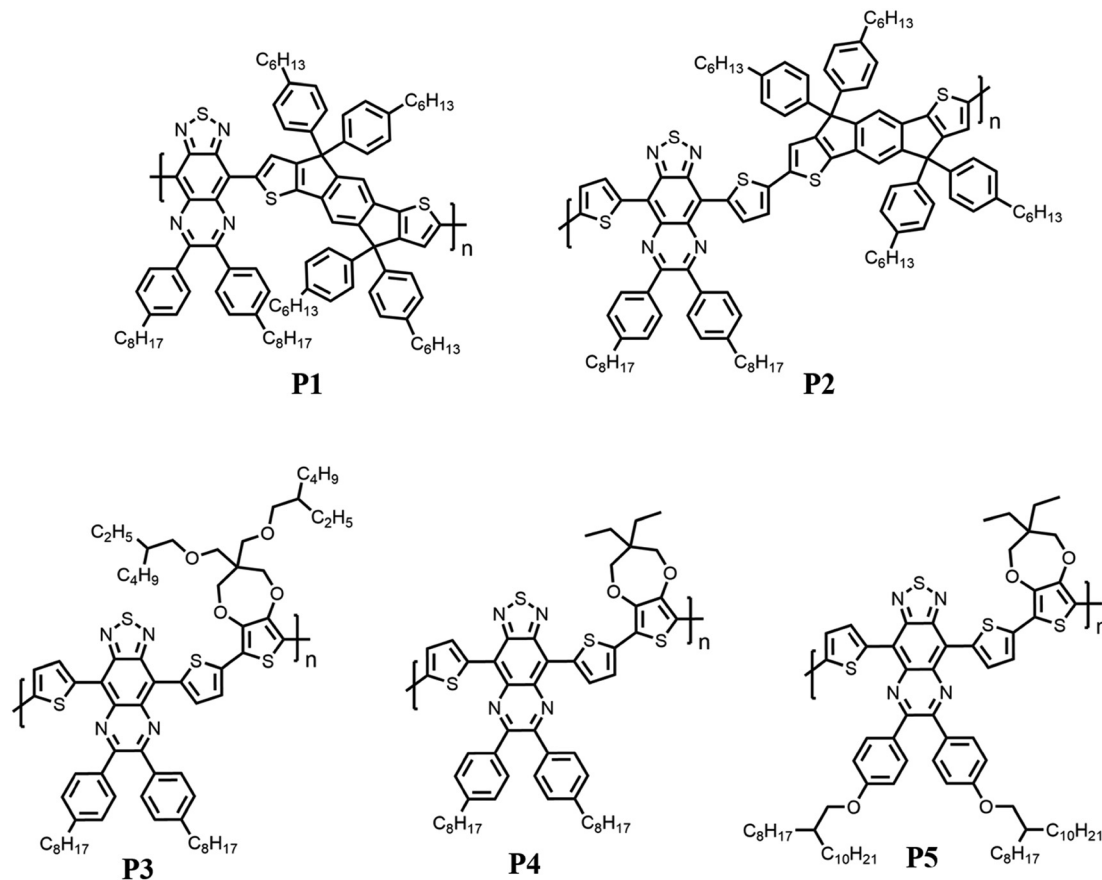
Andersson and co-workers demonstrated that a polymer based on TQ as the acceptor-unit and thiophene as the donor-unit exhibited a $\lambda_{max} = 1476$ nm, with a very low band gap $\lesssim 0.7$ eV.[14] In 2018, Ng et. al. reported a high efficiency shortwave infrared photodiode based on TQ and a cyclopentadithiophene derivative exhibiting high external quantum efficiency (EQE) of 35% at 1100 nm under −1 V, and photoresponse extending up to 1400 nm.[15] Soon after, Maes et. al. achieved a good EQE of 18% at 1130 nm at a −2 V bias in an OPD using a polymer based on TQ acceptor and terthiophene donor.[13] The OPD showed low dark current resulting in a high detectivity of 10^{10} Jones up to 1400 nm, and the photoresponse extended up to 1500 nm. Leem and co-workers reported an OPD with a similar polymer based on a TQ acceptor and terthiophene donor, but with different solubilizing groups, pushing the absorption wavelength further to 1200 nm with an excellent EQE of 22% at −1 V bias and a detectivity of 10^{10} Jones.[16] The same year Gasparani et. al. incorporated a polymer with TQ as the acceptor and a thiophene donor into an OPD which exhibited good responsivity of 0.03 A W^{-1} at 1200 nm and at −2 V bias was able to detect light up to 1800 nm.[17] However, the devices displayed low EQEs and relatively high dark currents (10^{-3} mA cm^{-2}) which is likely due to the polymer's extremely narrow band gap. Very recently, Tao and colleagues showed that introducing an n-type polymer N2200 interlayer in NIR-OPDs between the cathode and the active layer was effective at suppressing dark current (10^{-4} mA cm^{-2} at a low bias of −0.2 V) by two orders of magnitude in OPDs compared to the control device without N2200. The EQE was about 6–7% at 1300 nm at the same reverse bias.[18]

In this work, we report SWIR OPDs based on conjugated co-polymers with para-alkylpheny-substituted TQ as the acceptor unit. The donor units are based on 4,4,9,9-tetrakis(4-hexylphenyl)-4,9-dihydro-s-indaceno[1,2-b:5,6-b′]dithiophene (IDT) (P1, P2) and 3,4-dihydro-2H-thieno[3,4-b][1,4]dioxepine (ProDOT) (P3–P5). We assess the impact of different donors on the optoelectronic properties and the device performance in SWIR OPDs. Among them, the TQ-ProDOT polymer P3 blended with [6,6]-phenyl-C$_{71}$-butyric acid methyl ester (PC$_{71}$BM) exhibits the greatest EQE of 7.3% at 1200 nm under the reverse bias of −5 V with a ZnO electron transporting layer (ETL) whereas P5 instead results in the greatest shot noise approximated specific detectivity (D^*) of 1.9×10^{12} Jones at 0 V and 2.0×10^{10} Jones at −1 V due to its well-suppressed dark current, which rivals the highest performing OPDs to date (Table S3). However, care should be taken when comparing D^* values since they are reported at different bias voltages and calculated using different methods.[19,20] As the solubilizing groups and copolymerizing comonomers all have great impacts on the inherent properties of TQ-based polymers, it provides a vast chemistry space for tuning the bandgaps, energy levels, and solution processability of the resulting organic semiconductors to achieve high-performance shortwave infrared photodetectors.

Results and discussion

Scheme 1 displays the chemical structures of DA-type TQ-based polymers P1–P5, each incorporating different donors. They were synthesized via standard Stille-coupling reactions (Scheme S1). In the case of P1 and P2, we selected the moderate strength donor IDT to co-polymerize with the strong acceptor TQ (substituted with octylphenyl solubilizing groups). We avoided choosing too strong a donor to safeguard against achieving a band gap that was too narrow and could cause photoconductivity. Additionally, IDT has been used in high-efficiency polymer solar cells, owing to its large rigidified and co-planar fused aromatic structure, which restricts rotational motion and leads to lower reorganization energy.[21,22] Upon synthesis, however, the polymers P1 and P2 displayed wider band gaps than the values predicted by density functional theory (DFT) calculations (vide infra). Thus, to achieve narrower bandgaps for polymers P3 and P4, we employed stronger ProDOT-based donor units with their solubilizing groups specially designed for solution processability. Moreover, the propylenedioxy groups can promote backbone planarity via O···S interactions. GPC measurements for all polymers were carried out in trichlorobenzene at 135 °C to assess their molecular weights (Table 1). P1 displayed a high M_n of 63.5 kDa. Adding a thiophene spacer between TQ and IDT in P2 resulted in a higher M_n of 94.2 kDa, attributed to reduced steric hindrance in the coupling reaction. P3 had a relatively lower M_n of 11.0 kDa because the distannylated ProDOT co-monomer (10), being an oil at room temperature, was difficult to purify. To overcome this, we employed a ProDOT donor with shorter alkyl chains (12) which was solid at room temperature and thus was easily purified by recrystallization. We also hypothesized the shorter alkyl chains could also lead to enhanced aggregation in solution. Unfortunately, the resulting polymer P4 exhibited poor solubility, and precipitated out during polymerization. Only a small fraction of P4 could be extracted with o-dichlorobenzene, and this fraction exhibited a low M_n of 7.75 kDa and a narrow PDI of 1.12. P1–P3 had excellent solubility in chloroform. To improve solubility of P4, we synthesized P5 which employs a TQ acceptor bearing larger solubilizing groups (((2-octyldodecyl)oxy)phenyl) (15) co-polymerized with donor 12. For the purification of P5, we further fractionated the CH$_2$Cl$_2$ fraction by Soxhlet extraction using a mixture of hexanes and CHCl$_3$ at different ratios and selected the fraction that delivered the best performance for subsequent studies (see Synthesis section in the SI for details). This fraction, the third highest in molecular weight, had an M_n of 12.3 kDa and a PDI of 1.63, and displayed excellent solubility in chloroform even at room temperature. This is consistent with our expectation that higher purity monomers would improve polymerization efficiency, as the fraction with the third-highest M_n of P5 still exceeds the highest M_n fraction of P3. The thermal properties of the polymers were studied by thermogravimetric analysis (TGA) and density scanning calorimetry (DSC). TGA demonstrated that polymers P1–P3, and P5 exhibit high thermal stability under nitrogen, with onset decomposition temperatures (defined as 1% weight loss) of 330,

This journal is © The Royal Society of Chemistry 2025

J. Mater. Chem. C, 2025, **13**, 20760–20768 | **20761**

Scheme 1 Structures of the TQ-based polymers **P1–P5**.

349, and 328, and 340 °C, respectively (Fig. S1). DSC analysis revealed no discernable glass transitions for **P1–P3**. **P3** exhibited a small peak around 10 °C on the heating scan and a corresponding peak at 34 °C on the cooling scan, attributed to the melting and crystallization of the side chains, respectively, and **P5** exhibited a glass transition temperature around 177 °C. (Fig. S2). X-ray diffraction (XRD) study of all polymer films spin-coated on silicon substrates revealed no observable diffraction peaks (Fig. S3), suggesting they lack ordered crystalline structures, consistent with the absence of crystallization transitions in the DSC data.

The absorption spectra of the pristine polymer films are displayed in Fig. 1(a) and the corresponding data are summarized in Table 1. All five polymers exhibit low-energy absorptions which are assigned to the intra-molecular charge transfer (CT)

interaction between electron rich and deficient units. **P1** exhibits a peak absorption (λ_{max}) at 1028 nm with an optical band gap (E_g) of 1.06 eV, which we estimated from the low-energy band edge. Adding a thiophene spacer between TQ and IDT in **P2** blue shifts the low-energy λ_{max} to 938 nm, with a corresponding E_g of 1.08 eV. It is interesting to point out that adding a thiophene spacer blue-shifts the absorption despite thiophene being a stronger donor than IDT. We attribute this to the higher planarity of **P1**, which is disrupted by adding a thiophene in **P2**. Polymers **P3–P5** displayed similar optical properties exhibiting the most red-shifted absorptions with λ_{max} at 1166, 1188, and 1174 nm, and the narrowest band gaps of 0.87, 0.85, and 0.89 eV, respectively, as a result of the strong electron-donating properties of ProDOT and enhanced planarity which

Table 1 GPC, optical, and electrochemical properties of **P1–P5**

	$M_n{}^a$ (kDa)	PDI^a	Film λ_{max} (nm)	Solution λ_{max} (nm)	$\varepsilon \times 10^5$ (M^{-1} cm^{-1})	$E_g^{opt\,b}$ (eV)	$E_{HOMO}^{CV\,c}$ (eV)	$E_{LUMO}^{CV\,c}$ (eV)	E_g^{CV}
P1	75.0	2.44	1028	992	0.59	1.06	−5.21	−3.95	1.26
P2	94.2	1.88	940	908	0.46	1.08	−5.25	−3.90	1.35
P3	11.0	1.35	1166	1098	0.32	0.87	−4.86	−3.67	1.19
P4	7.75	1.12	1188	1124	0.19	0.85	N/A^d	−3.71	N/A^d
P5	12.3^e	1.63	1174	1132	0.47	0.89	−4.77	−3.65	1.12

^{a} Number average molecular weight and polydispersity index. ^{b} The optical energy gap was estimated from the onset of the low-energy band edge of pristine polymer films. ^{c} HOMO/LUMO energies were estimated from the oxidation and reduction potentials *vs.* Fc/Fc$^+$, respectively, as $-(eE_{onset} + 4.7 \text{ eV})$. ^{d} The oxidation wave was not observed. ^{e} Corresponds to the 3 : 2 Hex : CHCl$_3$ fraction (see synthesis section of SI for more details).

20762 | *J. Mater. Chem. C*, 2025, **13**, 20760–20768

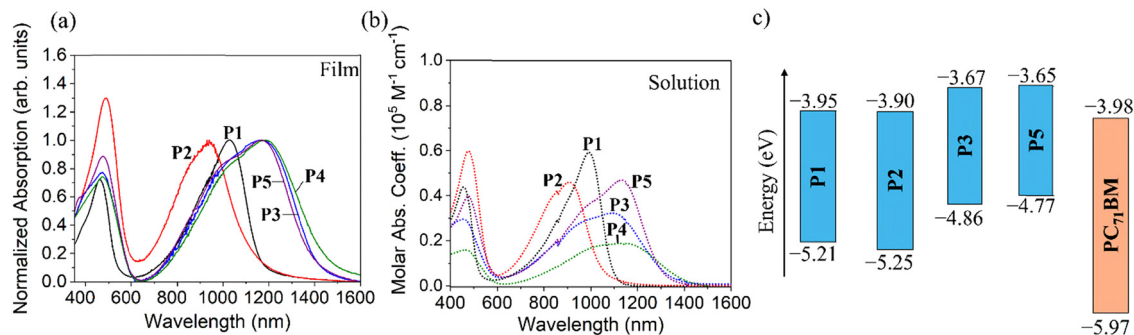This journal is © The Royal Society of Chemistry 2025

Fig. 1 (a) Normalized thin film UV-vis spectra of **P1–P5**. (b) Solution UV-vis spectra of **P1–P5** measured in CHCl$_3$ (c) Energy levels of films of donor polymers **P1–P3** and **P5** and the acceptor PC$_{71}$BM determined by cyclic voltammetry in MeCN. HOMO/LUMO energies were estimated from the oxidation and reduction potentials *vs.* Fc/Fc$^+$, respectively, as $-(eE_{onset} + 4.7\ eV)$.

is afforded by the O⋯S interactions between ProDOT and neighboring thiophene groups. Compared to the solution absorption spectra (Fig. 1(b)) the low-energy λ_{max} of the pristine films of **P1–P5** are red-shifted by 36, 32, 68, 64, and 42 nm, respectively. In solution, polymer **P1** exhibits the highest molar extinction coefficient which we attribute to greater HOMO–LUMO orbital overlap resulting from enhanced backbone co-planarity enforced by noncovalent S⋯N and H⋯N interactions between TQ and IDT. Meanwhile, the greater red-shifts of **P3–P5** compared with **P1–P2** are due to the stronger donor units in the former, resulting in stronger D–A interactions. The stronger absorption exhibited by **P5** compared to **P3** likely arises from the alkoxy groups attached to the TQ units which enlarges its conjugation system.

Cyclic voltammograms of pristine films of **P1–P3** and **P5** are shown in Fig. S4. We estimated the HOMO/LUMO energies (Fig. 2(b)) from the oxidation/reduction onset potentials, respectively. The HOMO energies were determined to be −5.21, −5.25, and −4.86 eV for **P1–P3**, respectively, and −4.77 for **P5**. We were unable to obtain a voltammogram with a well-defined oxidation wave for **P4**. The reason is not very clear. It may be due to doping or side reactions occurring during Soxhlet extraction using a high boiling point solvent, *o*-dichlorobenzene. The significantly lower oxidation potentials of **P3** and **P5** are a result of the stronger electron-donating properties of ProDOT compared to IDT. The estimated LUMO energies of **P1–P5** were −3.95, −3.90, −3.67, −3.71, and −3.65 eV respectively. This gives electrochemical band gaps of 1.26, 1.35, and 1.19 eV for **P1–P3**, respectively, and 1.12 eV for **P5**, which matches the trend seen in the optical band gaps.

Gas phase DFT calculations were carried out to evaluate the electronic properties of polymers **P1–P3** and **P5** (Table 2). To model the polymer backbones, we used oligomer chains with four repeat units, approximately where chain length saturation occurs for donor–acceptor type polymers.[23] The polymers based on the stronger ProDOT donor (**P3**, **P5**) exhibit shallower HOMO and LUMO energies and narrower band gaps than the IDT-based analogues (**P1** and **P2**), in agreement with cyclic voltammetry data. The calculations also reveal that the electron-donating alkoxy group on **P5** raises the HOMO energy by *ca.* 0.1 eV compared to its analogue **P3**. The ProDOT-containing polymers **P3** and **P5** exhibit enhanced planarity in their donor blocks and display dihedral angles of 1–4° (between

thiophene and ProDOT) enforced by O⋯S interactions with distance of 2.94 Å which is shorter than the sum of the van der Waals radii of S and O (3.32 Å). On the other hand, **P2**, which lacks such interactions, displays a dihedral angle of 4–12° between thiophene and IDT (Fig. S5).

These four donor polymers were used in the active layer of inverted bulk heterojunction (BHJ) OPDs to evaluate their photodetection performance. The OPD structure used for these investigations is: indium tin oxide (ITO)/ZnO/BHJ/MoO$_x$/Ag where the BHJ consists of a 1 : 3 D : A ratio of **P1–P3**, **P5** and PC$_{71}$BM. An energy level diagram is depicted in Fig. 2 along with current density–voltage (*J–V*) curves of the devices based on **P1–P3**, **P5** in the dark and under illumination at near their peak response wavelength. In general, **P2** devices exhibited the lowest dark current density among the set, measured to be 1.6 × 10^{-10} A cm^{-2} at 0 V which increased to 7.6 × 10^{-10} A cm^{-2} with −1 V reverse bias and 1.5 × 10^{-8} A cm^{-2} with −3 V reverse bias. The **P1** devices were less successful at suppressing charge injection under reverse bias with dark current density measured to be 8.6 × 10^{-11} A cm^{-2} at 0 V and increased substantially with an applied bias up to 2.0 × 10^{-6} A cm^{-6} at −1 V and 2.4 × 10^{-4} A cm^{-2} at −3 V. The dark current density of **P1** devices are 100× greater than **P2** at −1 V and 10 000× greater at −3 V despite their similar HOMO and LUMO energy levels. We primarily attribute this difference to the active layer film roughness which was measured to be 31.4 nm (root mean square roughness, RMS) for **P1**:PC$_{71}$BM and 1.8 nm for **P2**:PC$_{71}$BM by AFM (Fig. S6), not only indicating differences in the active layer morphology and D–A interactions but also introducing additional electron leakage pathways through direct contact between the active layer and Ag through the 10 nm MoO$_x$ layer. The **P3** devices demonstrated greater dark current density than **P1** or **P2**, measured to be 6.8 × 10^{-8} A cm^{-2} at 0 V, 2.5 × 10^{-4} A cm^{-2} at −1 V, and 5.3 × 10^{-4} A cm^{-2} at −3 V. While its dark current density begins at a higher value than **P1** and **P2**, its dependence on the applied bias is less significant as it only increases 2.1× as the bias increases from −1 V to −3 V as opposed to 1200× for **P1** and 200× for **P2** over that same range. Despite comparable energy levels to **P3**, **P5** devices exhibit substantially lower dark current density of 1.8 × 10^{-10} A cm^{-2} at 0 V, 3.3 × 10^{-6} A cm^{-2} at −1 V, and 2.2 × 10^{-5} A cm^{-2} at −3 V.

This journal is © The Royal Society of Chemistry 2025

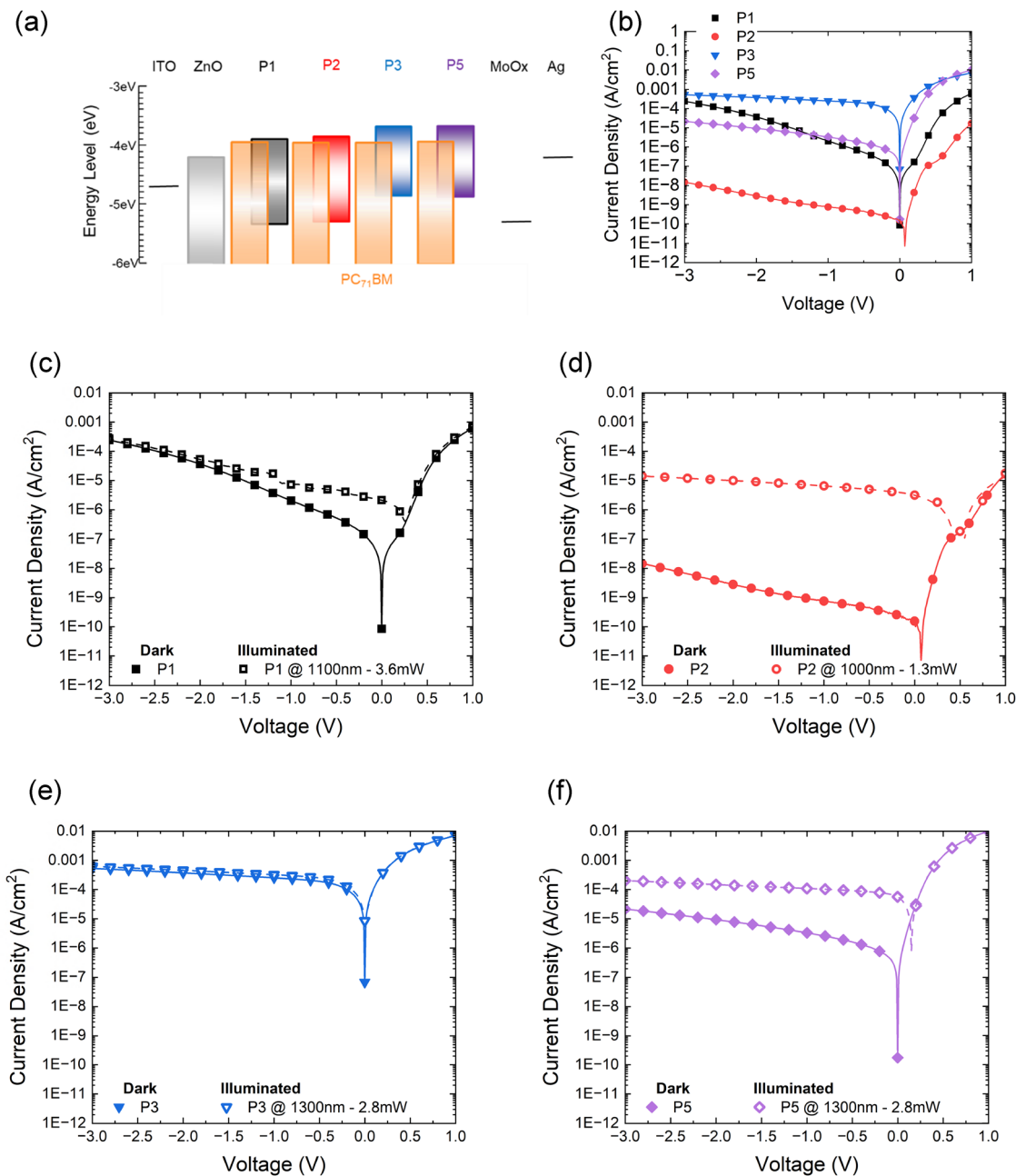*J. Mater. Chem. C*, 2025, **13**, 20760–20768 | **20763**

Fig. 2 (a) Energy level diagram for inverted BHJ OPDs with a **P1–P3**, **P5**:PC$_{71}$BM active layer. Polymer energy levels determined by cyclic voltammetry, while ITO, ZnO, MoO$_x$, and Ag referenced from literature.[24] (b) Dark current density vs voltage characteristics across inverted BHJ OPDs using **P1–P3**, **P5**. (c)–(f) Current density vs voltage characteristics in the dark without illumination (solid) and under illumination (open) near the maximum response wavelength for: (c) **P1**, (d) **P2**, (e) **P3**, and (f) **P5**.

In their analysis of the intrinsic detectivity limits of NIR OPDs, Gielen *et al.* found an apparent thermodynamic limit to dark current under conditions where the effective V_{OC} was less than 0.25. This typically encompasses systems where E_{CT} is less than 0.9 eV.[7] **P3** and **P5** active layers are expected to fall within this limit. In such cases, there is an exponential increase in the dark current limit with decreasing band gap from 10^{-6} A cm^{-2} at 0.9 eV to 10^{-4} A cm^{-2} at 0.7 eV when evaluated at -0.1 V. This is very similar to the 5×10^{-7} A cm^{-2} dark current density of **P5** measured at -0.1 V. While the shallower HOMO energy level of

P3 and **P5** than **P1** and **P2** (by roughly 0.4 eV) may contribute to increased leakage hole injection through the accessible ZnO ETL trap states under reverse bias conditions, this cannot account for the apparent suppression of this dark current in **P5** devices. The RMS roughness of **P3**:PC$_{71}$BM was measured to be 8.4 nm by AFM, which likely contributes to its elevated dark current. However, it remains smoother than **P1**:PC$_{71}$BM, so the roughness alone cannot account for the entirety of the high dark current. The **P5**:PC$_{71}$BM film is smoother with an RMS roughness of 4.1 nm. To further investigate the origin of the high dark

20764 | *J. Mater. Chem. C*, 2025, **13**, 20760–20768

This journal is © The Royal Society of Chemistry 2025

Table 2 DFT (B3LYP/6-311G*) calculations of HOMO, LUMO, HOMO–LUMO gap[a]

	HOMO (eV)	LUMO (eV)	E_g
P1	−4.36	−3.81	0.95
P2	−4.42	−3.87	1.00
P3	−4.27	−3.75	0.92
P5	−4.19	−3.68	0.91

[a] The HOMO was extracted from ground state B3LYP calculation, the LUMO from the αHOMO energy of the neutral triplet state, and the HOMO–LUMO gap from the first excitation energy from TD-DFT calculations. All calculations were carried out on the geometry optimized structures.[23]

current, space charge limited current (SCLC) mobility for each of the active layers was modeled by measuring conduction through single carrier devices using the Murgatroyd SCLC model (see Fig. S7 for details). Evaluated at an electric field of 10^5 V cm^{-1}, P3:PC$_{71}$BM exhibited the greatest μ_h of 2.1×10^{-3} cm^2 V^{-1} s^{-1} and a high μ_e of 1×10^{-3} cm^2 V^{-1} s^{-1} which are both two orders of magnitude greater than the comparable P5 active layer. Leakage charge carrier transport across the higher mobility P3 active layer is expected to lead to greater dark current magnitudes.

Capacitance–voltage measurements were also carried out on these devices to gain an understanding of the charge carrier properties behind these differences in dark currents, which have been included in Fig. S8. Mott–Schottky analysis is frequently used in semiconductors to determine dopant concentration, N, and has been extended to extract a trap state analog in undoped organic semiconductors through the equation:[25–28]

$$N_t = -\frac{2}{q\varepsilon_r\varepsilon_0}\left(\frac{d(C^{-2})}{dV}\right)^{-1} \quad (1)$$

where q is the elementary charge, ε_r is the relative permittivity of the medium, ε_0 is vacuum permittivity, and the last term is the slope of the Mott–Schottky plot of $1/C^2$ vs. V. Estimating the relative permittivity of the active layers to be 4.3 (a linear combination of 4.75 for PC$_{71}$BM and 3 for the donor polymers),[29] the 4 OPD N_t were calculated to be 7.6×10^{15} cm^{-3} for P1, 1.1×10^{16} cm^{-3} for P2, 2.6×10^{16} cm^{-3} for P3 and 1.6×10^{16} cm^{-3} for P5. The trend in trap density between the devices correlates to the order of their dark currents, with P3 > P5 > P2. While P1 does not fit the trend, its dark current is low at low bias, but rises rapidly with increasing bias. Since P1 is a rigid intrinsically microporous polymer, the roughness of the active layer contributes to additional leakage pathways. Devices with a P4 active layer were also fabricated and its dark current has been included in Fig. S9. However, the dark current density of these devices were several orders of magnitude greater than the P3 devices due in part to its lower molecular weight and poor solubility which resulted in much thinner active layers with poor quality. Ultimately, the devices were dominated by leakage current as seen in their symmetrical JV characteristics and their EQE could not be measured under an applied bias.

The photoresponse of the previous OPDs was measured and is depicted below in Fig. 3 in terms of EQE and responsivity as well as specific detectivity, determined by the shot noise

approximation. EQE, R, and D^* at notable reverse biases are presented in Table S2. Following the optical bandgap trends depicted in Fig. 1, the narrow bandgap P3 and P5 result in OPDs that exhibit the longest wavelength sensitivity with peak EQEs occurring at 1200 nm whereas P1 and P2 result in the shortest wavelength peak EQE at 850 nm. However, there are differences in the photosensitivity of P1 and P2 OPDs at longer wavelengths as the EQE of P1 remains flat until 1100 nm while the P2 cutoff begins at 1000 nm. Further differences in P1 and P2 are clear from the magnitude of their EQEs, 0.04% for P1 at a wavelength of 1100 nm and reverse bias of −1 V and 0.31% for P2 at a wavelength of 1000 nm and reverse bias of −1 V. As the reverse bias magnitude increases, the photocurrent of P1 becomes indistinguishable from the dark current and its EQE could not be determined while the EQE of P2 increases up to 1.2% at a wavelength of 1000 nm and a reverse bias of −5 V. The LUMO energy level of P1 is −3.95 eV which is very close to the −3.98 eV LUMO of PC$_{71}$BM so poor charge separation at the BHJ interface is a major contributor to its low EQE when used as a donor in this structure. Meanwhile, P2 with a LUMO energy of −3.90 eV appears to be slightly more sufficient at facilitating charge separation with PC$_{71}$BM than the P1 system and thus results in greater EQE. Furthermore, P1:PC$_{71}$BM exhibits the greatest disparity between μ_h and μ_e among the four OPDs which may lead to charge imbalances within the active layer, limiting EQE. Not only does the narrow bandgap of P3 result in the absorption of longer wavelength photons, but its shallow LUMO of −3.67 eV produces a 0.3 eV LUMO energy offset with PC$_{70}$BM which should efficiently separate excitons at the BHJ interface. This can be observed in the EQE of the P3 devices which are 2.4% at a wavelength of 1200 nm and reverse bias of −1 V which increases to 7.3% as the bias increases to −5 V. While the dark currents of P5 OPDs are greatly suppressed in comparison to P3, their EQE is slightly lower as well and calculated to be 2.1% at 1200 nm and a reverse bias of −1 V and 5.7% as the bias increases to −5 V. P5 exhibits greater EQE at 0 V than P3, but the two devices begin to diverge at high reverse bias which may be indicative of influences from the high dark currents of P3. The spectral response of P3 extends to lower energy photons than P5, with 3–4× greater EQE than P5 at 1400 nm, which may be a consequence of greater energetic disorder within the P3 active layer. While the LUMO energy level offset between the donor and acceptor is critical for this BHJ system, this becomes a challenge for OPDs with a SWIR sensitive donor as the narrow bandgap then necessitates a shallow HOMO energy level which appears to be susceptible to leakage carrier injection from the cathode.

The specific detectivity, D^*, of a photodetector can be used as a figure of merit expressing the capability of the device to measure low intensity signals via the noise-equivalent power, responsivity and normalized to device area. Under the shot noise limitation approximation, D^*_{sh} can be determined with the following equation:

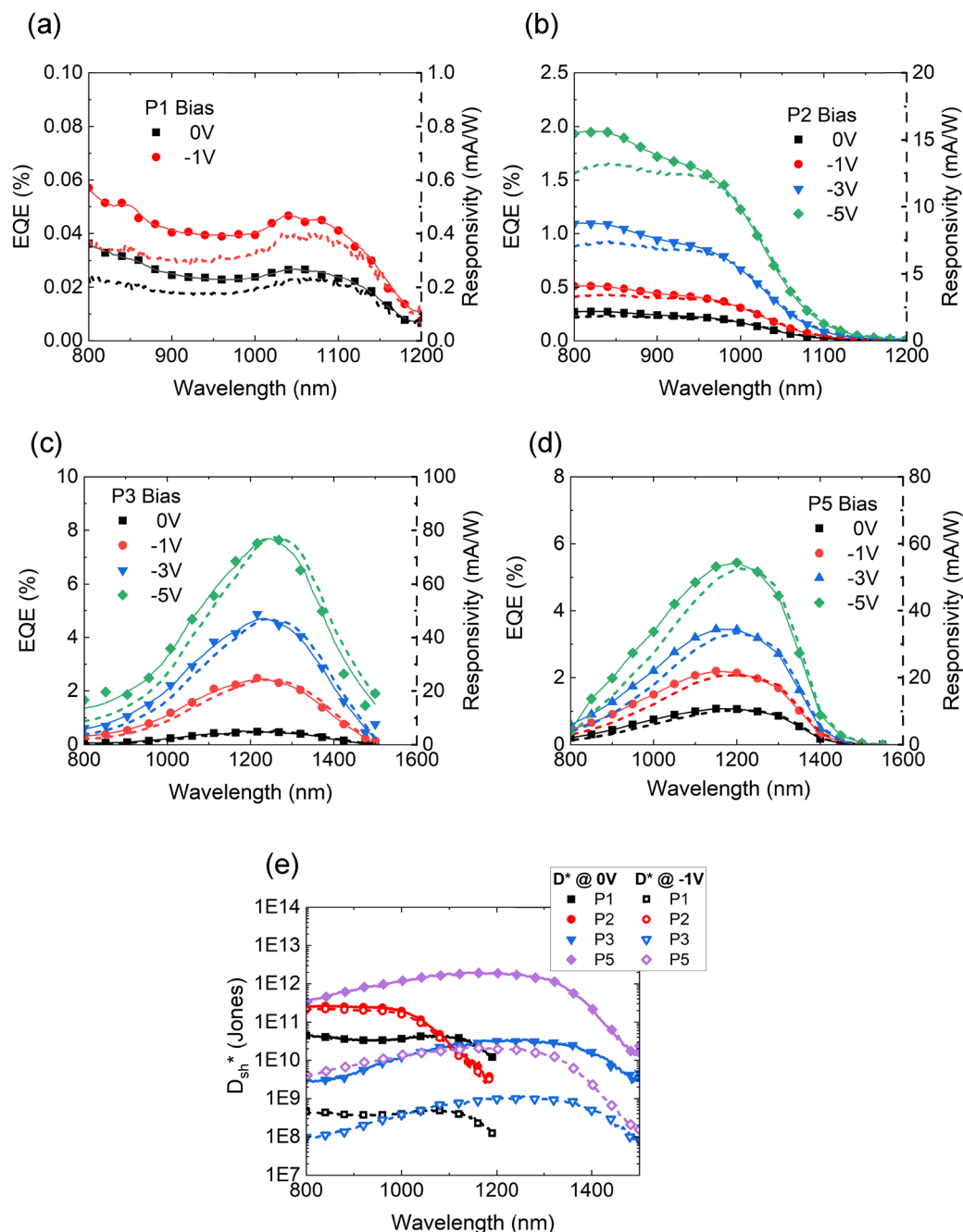$$D^*_{sh} = \frac{R}{\sqrt{2qJ_d}} \quad (2)$$

Fig. 3 EQE (solid) and responsivity (dash) characteristics of inverted BHJ OPDs with a: (a) **P1**:PC$_{71}$BM, (b) **P2**:PC$_{71}$BM, (c) **P1**:PC$_{71}$BM, and (d) **P1**:PC$_{71}$BM active layer under 0 V (black square), −1 V (red circle), −3 V (blue triangle), and −5 V (green diamond) bias conditions. (e) Shot noise approximated specific detectivity of the OPDs under 0 V (solid) and −1 V (dash) bias conditions.

where R is responsivity, q is the elementary charge, and J_d is the dark current density. It has been shown in literature that this approximation can lead to overestimations in $D^\star$ as, while shot noise may dominate the noise spectral density, the other noise effects influencing the spectral noise density can play a significant role.[19,27,30] Our effective currents near 0 V are much lower than the dark currents under reverse bias conditions, so we also calculated D_{sh}^* at −1 V for the devices in Fig. 3(e). At 1100 nm, **P1** D_{sh}^* (0 V) is calculated to be 4.0×10^{10} Jones and

D_{sh}^* (−1 V) is 4.5×10^8 Jones due to both its high dark currents and low responsivity. At 1000 nm, **P2** D_{sh}^* (0 V) is calculated to be 2.0×10^{11} Jones and D_{sh}^* (−1 V) is 1.6×10^{11} Jones, much greater than **P1** due to its lower dark current and greater responsivity. At 1200 nm, **P3** D_{sh}^* (0 V) is calculated to be 3.2×10^{10} Jones and D_{sh}^* (−1 V) is 1.0×10^9 Jones, less than the peak metrics of **P1** despite **P3**'s greater responsivity since its dark current is significantly greater. Up to 1400 nm, **P3** D_{sh}^* decreases only slightly, calculated to be 1.6×10^{10} Jones 0 V and

20766 | *J. Mater. Chem. C*, 2025, **13**, 20760–20768

This journal is © The Royal Society of Chemistry 2025

5×10^8 Jones at -1 V. At 1200 nm, **P5** D^*_{sh} (0 V) is calculated to be 1.9×10^{12} Jones and D^*_{sh} $(-1$ V) is 2.0×10^{10} Jones, owing to its significantly lower dark current than **P3** despite slightly lower responsivity. While the energy levels of **P3** and **P5** are comparable, owing to their similar donor–acceptor structure, the improved solubility from the addition of the bulky solubilizing agents to the TQ acceptor rather than the ProDOT donor appears to significantly improve the resulting device performance. **P5** devices exhibit lower dark currents and lower trap density than **P3**, with minimal effects on EQE and R. These results highlight how critical it is to address the high dark currents in SWIR sensitive OPDs, demonstrating **P5** as a viable donor with high shot noise approximated specific detectivity with room for further enhancements *via* optimizations in photocarrier extraction and EQE and additional approaches to reduce carrier leakage under reverse bias as well as other sources of high dark currents. Especially AFM images revealed that the morphology of the **P5**:PC$_{71}$BM active layer was not ideal and the domain sizes were a little bit too large. We are exploring various approaches to optimize its performance.

Conclusion

This work has demonstrated the use of thiadiazoloquinoxaline (TQ) as an electron-withdrawing unit and indacenodithiophene or propylenedioxythiophene as electron-donating units in the development of low-bandgap organic semiconductors for NIR-II photodetection. Five polymers were synthesized, with a maximum film absorption peak of 1188 nm (**P4**) and absorption tails beyond 1400 nm (**P3**, **P4** and **P5**). Materials showed good solubility, highlighted by the fabrication of organic photodiodes using films spin-coated at room temperature. These organic photodiodes highlighted the inherent challenges in low bandgap organic semiconductor photodetection, namely achieving high EQE with low dark current. The iterative improvement in material performance was evident, culminating in devices based on **P5** exhibiting the highest specific detectivity of 2.0×10^{10} Jones at -1 V (based on shot noise approximation). It is anticipated that this can be further improved with device optimization.

Conflicts of interest

There are no conflicts to declare.

Data availability

The data supporting the findings of this study are available within the article and supplementary information (SI). Experimental details of materials synthesis, device fabrication, and characterization, cyclic voltammograms, DFT optimized polymer backbone geometries, AFM images, and proton NMR spectra are included in the SI. See DOI: https://doi.org/10.1039/d5tc02404h.

References

1 Q. Li, Y. Guo and Y. Liu, *Chem. Mater.*, 2019, **31**, 6359–6379.
2 C. Wang, X. Zhang and W. Hu, *Chem. Soc. Rev.*, 2020, **49**, 653–670.
3 Kenry, Y. Duan and B. Liu, *Adv. Mater.*, 2018, **30**, 1802394.
4 G. Hong, A. L. Antaris and H. Dai, *Nat. Biomed. Eng.*, 2017, **1**, 0010.
5 P. C. Chow and T. Someya, *Adv. Mater.*, 2020, **32**, 1902045.
6 H. Anabestani, S. Nabavi and S. Bhadra, *Nanomaterials*, 2022, **12**, 3775.
7 S. Gielen, C. Kaiser, F. Verstraeten, J. Kublitski, J. Benduhn, D. Spoltore, P. Verstappen, W. Maes, P. Meredith and A. Armin, *Adv. Mater.*, 2020, **32**, 2003818.
8 J.-L. Brédas, D. Beljonne, V. Coropceanu and J. Cornil, *Chem. Rev.*, 2004, **104**, 4971–5004.
9 J. D. Yuen and F. Wudl, *Energy Environ. Sci.*, 2013, **6**, 392–406.
10 T. Mikie and I. Osaka, *J. Mater. Chem. C*, 2020, **8**, 14262–14288.
11 X. Ji and L. Fang, *Polym. Chem.*, 2021, **12**, 1347–1361.
12 E. Perzon, M. Andersson, F. Zhang, M. Andersson, O. Inganäs and W. Mammo, *Adv. Mater.*, 2007, 19.
13 F. Verstraeten, S. Gielen, P. Verstappen, J. Raymakers, H. Penxten, L. Lutsen, K. Vandewal and W. Maes, *J. Mater. Chem. C*, 2020, **8**, 10098–10103.
14 T. T. Steckler, P. Henriksson, S. Mollinger, A. Lundin, A. Salleo and M. R. Andersson, *J. Am. Chem. Soc.*, 2014, **136**, 1190–1193.
15 Z. Wu, Y. Zhai, W. Yao, N. Eedugurala, S. Zhang, L. Huang, X. Gu, J. D. Azoulay and T. N. Ng, *Adv. Funct. Mater.*, 2018, **28**, 1805738.
16 I. Park, C. Kim, R. Kim, N. Li, J. Lee, O. K. Kwon, B. Choi, T. N. Ng and D. S. Leem, *Adv. Opt. Mater.*, 2022, **10**, 2200747.
17 P. Jacoutot, A. D. Scaccabarozzi, T. Zhang, Z. Qiao, F. Aniés, M. Neophytou, H. Bristow, R. Kumar, M. Moser and A. D. Nega, *Small*, 2022, **18**, 2200580.
18 X. Yu, H. Lin, Z. He, X. Du, Z. Chen, G. Yang, C. Zheng and S. Tao, *ACS Appl. Mater. Interfaces*, 2023, **15**, 16918–16929.
19 I. K. Kim, J. H. Jo, J. B. Lee and Y. J. Choi, *Org. Electron.*, 2018, **57**, 89–92.
20 T. Shan, X. Hou, X. Yin and X. Guo, *Front. Optoelectron.*, 2022, **15**, 49.
21 I. McCulloch, R. S. Ashraf, L. Biniek, H. Bronstein, C. Combe, J. E. Donaghey, D. I. James, C. B. Nielsen, B. C. Schroeder and W. Zhang, *Acc. Chem. Res.*, 2012, **45**, 714–722.

This journal is © The Royal Society of Chemistry 2025

J. Mater. Chem. C, 2025, **13**, 20760–20768 | **20767**

22 Y. Li, M. Gu, Z. Pan, B. Zhang, X. Yang, J. Gu and Y. Chen, *J. Mater. Chem. A*, 2017, **5**, 10798–10814.

23 T. M. McCormick, C. R. Bridges, E. I. Carrera, P. M. DiCarmine, G. L. Gibson, J. Hollinger, L. M. Kozycz and D. S. Seferos, *Macromolecules*, 2013, **46**, 3879–3886.

24 Y.-C. Huang, T.-Y. Wang, Z.-H. Huang and S. R. M. S. Santiago, *ACS Appl. Mater. Interfaces*, 2024, 27576–27586.

25 A. D. Scaccabarozzi, A. Basu, F. Aniés, J. Liu, O. Zapata-Arteaga, R. Warren, Y. Firdaus, M. I. Nugraha, Y. Lin and M. Campoy-Quiles, *Chem. Rev.*, 2021, **122**, 4420–4492.

26 Y. Zhu, H. Chen, R. Han, H. Qin, Z. Yao, H. Liu, Y. Ma, X. Wan, G. Li and Y. Chen, *Natl. Sci. Rev.*, 2024, **11**, nwad311.

27 W. Zhong, X. Wang, W. Wang, Z. Song, Y. Tang, B. Chen, T. Yang and Y. Liang, *Adv. Sci.*, 2025, **12**, 2410332.

28 K. Sivula, *ACS Energy Lett.*, 2021, **6**, 2549–2551.

29 M. P. Hughes, K. D. Rosenthal, N. A. Ran, M. Seifrid, G. C. Bazan and T. Q. Nguyen, *Adv. Funct. Mater.*, 2018, **28**, 1801542.

30 J. Kublitski, A. Hofacker, B. K. Boroujeni, J. Benduhn, V. C. Nikolis, C. Kaiser, D. Spoltore, H. Kleemann, A. Fischer and F. Ellinger, *Nat. Commun.*, 2021, **12**, 551.

20768 | *J. Mater. Chem. C*, 2025, **13**, 20760–20768

This journal is © The Royal Society of Chemistry 2025